Available on the CERN CDS information server **CMS PAS FTR-18-034**

CMS Physics Analysis Summary

Contact: cms-phys-conveners-ftr@cern.ch

2022/04/26

Projection of the top quark spin correlation measurement and search for top squark pair production at the HL-LHC

The CMS Collaboration

Abstract

The CMS prospects for the high-luminosity phase of the LHC on the measurement of the top quark spin correlation is presented, using events containing two oppositely charged lepton pairs (eμ) produced in proton-proton collisions at a center-of-mass energy of 14 TeV assuming an integrated luminosity of 3 ab^{-1}. We investigate the normalised strength of the spin correlation in the sample and hence, provide a first performance study in future spin correlation measurements at 14 TeV. As an application, these observables are used in a Deep Neural Network to search for pair production of supersymmetric (anti-)top scalar quarks decaying into (anti-)top quarks and neutralinos, which escape the detector undetected. The observables sensitive to top quark spin correlation allow to study the corridor where the mass difference between the top scalar quark and the neutralino is about equal to the top quark mass. Compared to existing Run 2 results, this work will particularly push the discovery potential to the most natural top squark mass values below 300 GeV by one order of magnitude.

1 Introduction

The top quark is the heaviest known fundamental particle with a very short life time. Its decay width (Γ), slightly above 1 GeV, is larger than the QCD hadronization scale ($\lambda_{QCD} \lesssim 1$ GeV) and much larger than the spin decorrelation scale ($\lambda^2_{QCD}/m_t \sim 0.1$ MeV). Thus the top quark decays before hadronization and its spin information can be measured via angular distribution of its decay products. In order to cancel loop-order effects on the Higgs boson mass, presence of new physics (NP) effects can be expected in top quark production. In this case the spin information can be used to differentiate between standard model (SM) and NP production, that have very similar kinematics and final states.

Such a situation occurs in the case of top squark production, where a top squark ($\tilde{t}_1$) decays to a top quark and a neutralino ($\tilde{\chi}^0_1$) (see Figure 1), with the mass difference between the top squark and the neutralino approximately equal to the mass of the top quark. Searches for such top squarks are difficult to perform due to the rapidly changing detector efficiencies, leaving typically a weak discovery potential in the top squark and neutralino plane at low masses.

Since top squarks are scalar particles, the resulting spins of the daughter top quarks are basically uncorrelated, and therefore notably different from the spin correlation predicted in $\mathrm{t\bar{t}}$ pairs produced in the SM. Since the low mass top squark process has significant cross section it should provide an excess of $\mathrm{t\bar{t}}$ like events.

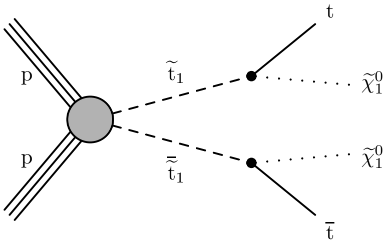

Figure 1: Feynmann diagram for the production of (anti-)top squark pairs decaying into (anti-)top quarks and neutralinos.

In this paper, we present a projection of how precise angular distributions of leptons stemming from the decay of top quarks can be measured at the HL-LHC for integrated luminosity of 3000 fb^{-1} at $\sqrt{s} = 14$ TeV and utilize that to extract the fraction of the strength of top quark spin correlation relative to the SM prediction. Second, as an application of utilizing such angular distributions, and to study a specific model that predicts zero spin correlation, a future search for supersymmetric (SUSY) top squark pair production in the dilepton final state is outlined. Projections of uncertainties that future analyses will face are made using Yellow Report recommendations [1].

2 Formalism and observables

The square of the matrix element for $\mathrm{t\bar{t}}$ production and decay to two leptons (with appropriate color and spin summation implied) [2] can be written as

$$|\mathcal{M}(\mathrm{q\bar{q}/gg} \to \mathrm{t\bar{t}} \to \ell^+\nu\mathrm{b}\ \ell^-\bar{\nu}\mathrm{\bar{b}})|^2 \propto \rho R \bar{\rho}. \quad (1)$$

Here, ℓ refers to an electron or muon, R is the spin density matrix related to on-shell $\mathrm{t\bar{t}}$ production, and ρ and $\bar{\rho}$ are the decay spin density matrices for the top quark and antiquark, respectively. The narrow width of the top quark compared to its mass allows factorization of the production and decay processes.

The R matrix is purely a function of the partonic initial state and production kinematic variables, and is therefore sensitive to beyond the standard model (BSM) phenomena in $\mathrm{t\bar{t}}$ production [2].

The production spin density matrix R can be decomposed in the t and $\mathrm{\bar{t}}$ spin spaces using the Pauli spin matrix basis:

$$R \propto \tilde{A}\mathbb{1}\otimes\mathbb{1} + \tilde{B}_i^{+}\sigma^i\otimes\mathbb{1} + \tilde{B}_i^{-}\mathbb{1}\otimes\sigma^i + \tilde{C}_{ij}\sigma^i\otimes\sigma^j, \tag{2}$$

where $\mathbb{1}$ is the 2×2 unit matrix, σ^i are the Pauli matrices, and the first (second) matrix in each tensor product refers to the top quark (antiquark) spin space. The function $\tilde{A}$ determines the total $\mathrm{t\bar{t}}$ production cross section and the top quark kinematic distributions, $\tilde{B}^{\pm}$ are three-dimensional vectors of functions that characterize the degree of top quark or antiquark polarization in each direction, and $\tilde{C}$ is a 3×3 matrix of functions that characterize the correlation between the top quark and antiquark spins.

We choose an orthonormal basis to decompose the top quark spin, where these functions have definite properties with respect to discrete symmetries [3, 4]. This basis is illustrated in Fig. 2. Working in the $\mathrm{t\bar{t}}$ center-of-mass (CM) frame, we use the helicity axis $\hat{k}$ defined by the top quark direction and the direction $\hat{p}$ of the incoming parton to define the direction perpendicular to the scattering plane $\hat{n} = (\hat{p}\times\hat{k})/\sin\Theta$, where Θ is the top quark scattering angle. The direction in the scattering plane mutually perpendicular to $\hat{k}$ and the transverse axis $\hat{n}$ is given by $\hat{r} = (\hat{p} - \hat{k}\cos\Theta)/\sin\Theta$.

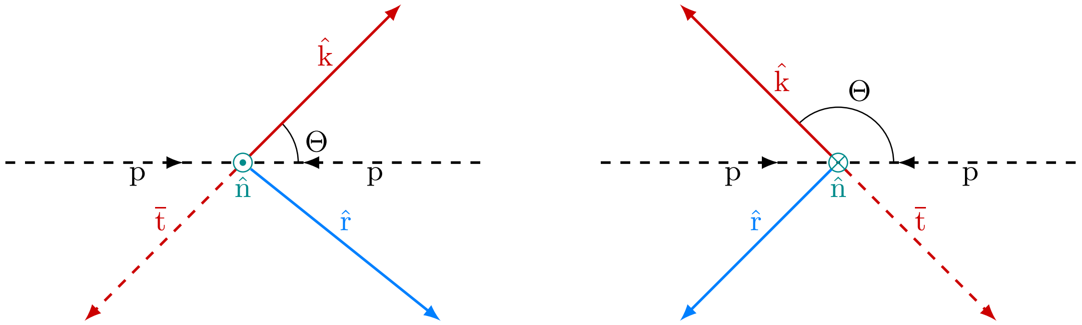

Figure 2: Coordinate system used for the spin measurements, illustrated in the scattering plane for $\Theta < \pi/2$ (left) and $\Theta > \pi/2$ (right), where the signs of $\hat{r}$ and $\hat{n}$ are flipped at $\Theta = \pi/2$ as shown in Eq. (4). The $\hat{k}$ axis is defined by the top quark direction, measured in the $\mathrm{t\bar{t}}$ CM frame. For the basis used to define the coefficient functions in Eq. (3), the incoming particles p represent the incoming partons, while for the basis used to measure the coefficients in Eqs. (8)–(10) they represent the incoming protons.

We expand $\tilde{B}_i^{\pm}$ and $\tilde{C}_{ij}$ in terms of the orthonormal basis $\{\hat{k}, \hat{r}, \hat{n}\}$:

$$\begin{aligned}
\tilde{B}_i^{\pm} &= b_k^{\pm}\hat{k}_i + b_r^{\pm}\hat{r}_i + b_n^{\pm}\hat{n}_i, \\
\tilde{C}_{ij} &= c_{kk}\hat{k}_i\hat{k}_j + c_{rr}\hat{r}_i\hat{r}_j + c_{nn}\hat{n}_i\hat{n}_j \\
&\quad + c_{rk}(\hat{r}_i\hat{k}_j + \hat{k}_i\hat{r}_j) + c_{nr}(\hat{n}_i\hat{r}_j + \hat{r}_i\hat{n}_j) + c_{kn}(\hat{k}_i\hat{n}_j + \hat{n}_i\hat{k}_j) \\
&\quad + c_n(\hat{r}_i\hat{k}_j - \hat{k}_i\hat{r}_j) + c_k(\hat{n}_i\hat{r}_j - \hat{r}_i\hat{n}_j) + c_r(\hat{k}_i\hat{n}_j - \hat{n}_i\hat{k}_j).
\end{aligned} \tag{3}$$

The coefficient functions $b_i^{\pm}$, c_{ij}, and c_i are functions of the partonic CM energy squared s and $\cos\Theta$.

The Bose–Einstein symmetry of the gg initial state requires a redefinition of the $\hat{r}$ and $\hat{n}$ axes (which are odd under Bose–Einstein symmetry) to allow nonzero values of the relevant coefficient functions [4]:

$$\{\hat{k}, \hat{r}, \hat{n}\} \to \{\hat{k},\ \mathrm{sign}(\cos\Theta)\hat{r},\ \mathrm{sign}(\cos\Theta)\hat{n}\}, \tag{4}$$

i.e., we have used the sign of the cosine of the top quark scattering angle, which is odd under Bose–Einstein symmetry, to define a "forward" direction for each event.

The top quark spin cannot be measured directly, but the angular distribution of the decay products of a top quark is correlated with its spin axis [5]:

$$\frac{1}{\Gamma}\frac{\mathrm{d}\Gamma}{\mathrm{d}\cos\chi_a} = \frac{1}{2}\left(1 + \kappa_a \cos\chi_a\right), \tag{5}$$

where Γ is the top quark decay width, χ_a is the angle between the direction of decay product a and the top quark spin axis in the top quark rest frame, and κ_a is the spin analyzing power. The charged lepton has maximal spin analyzing power, $\kappa_{\ell^+} \lesssim 1$ [6]. For top antiquark decay, the sign is reversed: $\kappa_{\ell^-} = -\kappa_{\ell^+}$.

Each of the 15 coefficient functions from Eq. (3) (six $b_i^{\pm}$ and nine $c_{ij/i'}$) is probed by detector level events counts, using the charged lepton directions measured in the rest frames of their parent top quark and antiquark as proxies for the top quark and antiquark spins. Since the measurements are made in pp collisions, the basis is adjusted from that of Eq. (4) by defining $\hat{p} = (0, 0, 1)$, the direction of the proton beam in the positive z direction in the laboratory frame, in the derivation of $\hat{r}$ and $\hat{n}$ [4].

The four-fold angular distribution for the two leptons follows from Eqs. (1) and (2), and is given by

$$\frac{1}{\sigma}\frac{\mathrm{d}^4\sigma}{\mathrm{d}\Omega_1\,\mathrm{d}\Omega_2} = \frac{1}{(4\pi)^2}\left(1 + B_1 \cdot \hat{\ell}_1 + B_2 \cdot \hat{\ell}_2 - \hat{\ell}_1 \cdot C \cdot \hat{\ell}_2\right), \tag{6}$$

where σ is the $\mathrm{t\bar{t}}$ production cross section, $\Omega_{1,2}$ are the solid angles of the leptons in their parent top quark and antiquark rest frames, and $\hat{\ell}_{1,2}$ are the corresponding unit vectors. The negative sign in front of the matrix C is chosen to define same-helicity top quarks as having positive spin correlation. The elements of the vectors $B_{1,2}$ and the matrix C are the following coefficients [in whose definitions the factors of κ_{ℓ^+} and κ_{ℓ^-} from Eq. (5) are absorbed]:

- B_1^i and B_2^i, the top quark and antiquark polarization coefficients with respect to each reference axis i (sensitive to b_i^+ and b_i^-);
- C_{ii}, the "diagonal" spin correlation coefficient for each reference axis i (sensitive to c_{ii});
- C_{ij}, the "cross" spin correlation coefficients for each pair of axes $i \neq j$, whose sums and differences $C_{ij} \pm C_{ji}$ are sensitive to c_{ij} and $c_{i'}$

These measurable coefficients are closely related to the production spin density matrix coefficient functions from Eq. (3), but are not identical, owing to the different basis used for the spin measurement. We do not measure the coefficients differentially or attempt to separate the contributions from different initial states. The association between the measured coefficients and the coefficient functions is given in Table 1.

For each of the 15 coefficients that make up $B_{1,2}$ and C, a change of variables can be made to obtain a single-differential cross section that depends only on that coefficient. After integrating out the azimuthal angles, Eq. (6) reduces to

$$\frac{1}{\sigma}\frac{\mathrm{d}^2\sigma}{\mathrm{d}\cos\theta_1^i\,\mathrm{d}\cos\theta_2^j} = \frac{1}{4}\left(1 + B_1^i\cos\theta_1^i + B_2^j\cos\theta_2^j - C_{ij}\cos\theta_1^i\cos\theta_2^j\right), \tag{7}$$

where θ_1^i (θ_2^j) is the angle of the positively (negatively) charged lepton, measured with respect to axis i (j) in the rest frame of its parent top quark (antiquark). By changing variables (if necessary) and integrating out one of the angles, we can derive single-differential cross sections with respect to $\cos\theta_1^i$, $\cos\theta_2^i$, and $\cos\theta_1^i\cos\theta_2^j$:

$$\begin{aligned}\frac{1}{\sigma}\frac{\mathrm{d}\sigma}{\mathrm{d}\cos\theta_1^i} &= \frac{1}{2}\left(1 + B_1^i\cos\theta_1^i\right),\\ \frac{1}{\sigma}\frac{\mathrm{d}\sigma}{\mathrm{d}\cos\theta_2^i} &= \frac{1}{2}\left(1 + B_2^i\cos\theta_2^i\right),\\ \frac{1}{\sigma}\frac{\mathrm{d}\sigma}{\mathrm{d}\cos\theta_1^i\cos\theta_2^j} &= \frac{1}{2}\left(1 - C_{ij}\cos\theta_1^i\cos\theta_2^j\right)\ln\left(\frac{1}{|\cos\theta_1^i\cos\theta_2^j|}\right).\end{aligned} \tag{8}$$

Similarly, starting from Eq. (6), we obtain (for $i \neq j$)

$$\begin{aligned}\frac{1}{\sigma}\frac{\mathrm{d}\sigma}{\mathrm{d}x_\pm} &= \frac{1}{2}\left(1 - \frac{C_{ij}\pm C_{ji}}{2}\,x_\pm\right)\cos^{-1}|x_\pm|,\\ x_\pm &= \cos\theta_1^i\cos\theta_2^j \pm \cos\theta_1^j\cos\theta_2^i.\end{aligned} \tag{9}$$

Thus, in order to determine the 15 coefficients, detector level event counts are measured as a function of the following 15 observables:

- the three $\cos\theta_1^i$ terms and three $\cos\theta_2^i$ terms to measure B_1^i and B_2^i, the top quark and antiquark polarization coefficients with respect to each reference axis i;
- the three $\cos\theta_1^i\cos\theta_2^i$ terms to measure C_{ii}, the diagonal spin correlation coefficient for each axis i;
- the six sum and difference terms $\cos\theta_1^i\cos\theta_2^j \pm \cos\theta_1^j\cos\theta_2^i$ to measure $C_{ij} \pm C_{ji}$, the sums and differences of the cross spin correlation coefficients for each pair of axes $i \neq j$.

The spin correlation coefficient D is related to the diagonal C coefficients as $D = -\mathrm{Tr}[C]/3 = -(C_{kk} + C_{rr} + C_{nn})/3$. We make a direct measurement of the D coefficient using the distribution of the dot product of the two lepton directions measured in their parent top quark and antiquark rest frames [4], $\hat{\ell}_1 \cdot \hat{\ell}_2 = \cos\varphi$:

$$\frac{1}{\sigma}\frac{\mathrm{d}\sigma}{\mathrm{d}\cos\varphi} = \frac{1}{2}(1 - D\cos\varphi). \tag{10}$$

We also measure three related laboratory-frame distributions, using the following observables:

- $\cos\varphi_{\mathrm{lab}} = \hat{\ell}_1^{\mathrm{lab}} \cdot \hat{\ell}_2^{\mathrm{lab}}$, defined by analogy to $\cos\varphi$, but using the lepton directions measured in the laboratory frame, which have excellent experimental resolution;
- $|\Delta\phi_{\ell\ell}|$, the difference in azimuthal angle ϕ between the two leptons in the laboratory frame (whose shape is partly dependent on the above coefficients, particularly the $C(i,i)$, and has excellent experimental resolution);
- $|\Delta\eta_{\ell\ell}|$, the difference in pseudorapidity between the two leptons.

Table 1: Observables and corresponding coefficients and production spin density matrix coefficient functions. For the laboratory-frame asymmetries shown in the last three rows, there is no direct correspondence with the coefficient functions.

Observable	**Coefficient**	**Coefficient function**
$\cos\theta_1^k$	B_1^k	b_k^+
$\cos\theta_2^k$	B_2^k	b_k^-
$\cos\theta_1^r$	B_1^r	b_r^+
$\cos\theta_2^r$	B_2^r	b_r^-
$\cos\theta_1^n$	B_1^n	b_n^+
$\cos\theta_2^n$	B_2^n	b_n^-
$\cos\theta_1^k \cos\theta_2^k$	C_{kk}	c_{kk}
$\cos\theta_1^r \cos\theta_2^r$	C_{rr}	c_{rr}
$\cos\theta_1^n \cos\theta_2^n$	C_{nn}	c_{nn}
$\cos\theta_1^r \cos\theta_2^k + \cos\theta_1^k \cos\theta_2^r$	$C_{rk} + C_{kr}$	c_{rk}
$\cos\theta_1^r \cos\theta_2^k - \cos\theta_1^k \cos\theta_2^r$	$C_{rk} - C_{kr}$	c_n
$\cos\theta_1^n \cos\theta_2^r + \cos\theta_1^r \cos\theta_2^n$	$C_{nr} + C_{rn}$	c_{nr}
$\cos\theta_1^n \cos\theta_2^r - \cos\theta_1^r \cos\theta_2^n$	$C_{nr} - C_{rn}$	c_k
$\cos\theta_1^n \cos\theta_2^k + \cos\theta_1^k \cos\theta_2^n$	$C_{nk} + C_{kn}$	c_{kn}
$\cos\theta_1^n \cos\theta_2^k - \cos\theta_1^k \cos\theta_2^n$	$C_{nk} - C_{kn}$	$-c_r$
$\cos\varphi$	D	$-(c_{kk} + c_{rr} + c_{nn})/3$
$\cos\varphi_{\mathrm{lab}}$	$A_{\cos\varphi}^{\mathrm{lab}}$	—
$\lvert\Delta\phi_{\ell\ell}\rvert$	$A_{\lvert\Delta\phi_{\ell\ell}\rvert}$	—
$\lvert\Delta\eta_{\ell\ell}\rvert$	$\lvert\Delta\eta_{\ell\ell}\rvert$	—

The association between the 22 measured observables and the coefficients and coefficient functions is given in Table 1.

The observables defined here are used to build a neural network described in Section 6.

Few selected observables are also used to perform a measurement of the strength of the spin correlation relative to the SM prediction, described in Section 5.

3 The CMS Phase-2 Detector

The CMS detector [7] will be substantially upgraded in order to fully exploit the physics potential offered by the increase in luminosity, and to cope with the demanding operational conditions at the HL-LHC [8–12]. The upgrade of the first level hardware trigger (L1) will allow for an increase of L1 rate and latency to about 750 kHz and 12.5 μs, respectively, and the high-level software trigger (HLT) is expected to reduce the rate by about a factor of 100 to 7.5 kHz. The entire pixel and strip tracker detectors will be replaced to increase the granularity, reduce the material budget in the tracking volume, improve the radiation hardness, and extend the geometrical coverage and provide efficient tracking up to pseudorapidities of about $|\eta| = 4$. The muon system will be enhanced by upgrading the electronics of the existing cathode strip chambers (CSC), resistive plate chambers (RPC) and drift tubes (DT). New muon detectors based on improved RPC and gas electron multiplier (GEM) technologies will be installed to add redundancy, increase the geometrical coverage up to about $|\eta| = 2.8$, and improve the trigger and reconstruction performance in the forward region. The barrel electromagnetic calorimeter (ECAL) will feature the upgraded front-end electronics that will be able to exploit the information from single crystals at the L1 trigger level, to accommodate trigger latency and bandwidth requirements, and to provide 160 MHz sampling allowing high precision timing capability for photons. The hadronic calorimeter (HCAL), consisting in the barrel region of brass absorber plates and plastic scintillator layers, will be read out by silicon photomultipliers (SiPMs). The endcap electromagnetic and hadron calorimeters will be replaced with a new combined sampling calorimeter (HGCal) that will provide highly-segmented spatial information in both transverse and longitudinal directions, as well as high-precision timing information. Finally, the addition of a new timing detector for minimum ionizing particles (MTD) in both barrel and endcap regions is envisaged to provide the capability for 4-dimensional reconstruction of interaction vertices that will significantly offset the CMS performance degradation due to high pileup rates.

A detailed overview of the CMS detector upgrade program is presented in Ref. [8–15], while the expected performance of the reconstruction algorithms and pile-up mitigation with the CMS detector is summarised in Ref. [16].

4 Objects and Event Selection

The signal for this analysis is characterized by two oppositely-charged isolated leptons, one electron and one muon, and two jets of which at least one is b-tagged. Top quark pairs decaying into ee or $\mu\mu$ are not considered here since these two channels are affected by an increased amount of Drell-Yan background contributions, which deteriorate the sensitivity to new physics and the precision with which the spin correlation coefficient can be extracted. Even worse are decays of top quark pairs into lepton+jets or all-hadronic final states since these events not only suffer from increased amounts of background contributions, but also from a reduced spin analyzing power of the jets stemming from the decay of the W bosons.

Tau leptons decaying into electrons or muons are also treated as signal for this analysis. A large missing transverse energy ${E_T}^{miss}$ is also imposed. Events are selected with the following requirements :

- $p_T > 25(20)$ GeV for the leading (trailing) lepton and $|\eta| < 2.4$;
- in the case of electrons, we also reject those in the gap between the barrel and the endcap (i.e. $1.442 < |\eta| < 1.566$);

- the dilepton invariant mass $m_{\ell\ell} > 20$ GeV to suppress events from decays of heavy-flavor resonances.

In this analysis electrons are identified by selecting isolated electromagnetic clusters subtracted by charged hadron activity. In the case of muons, we select the tightest working point of a neural net based muon identification. In addition to the leptons, we require at least two jets clustered using the anti-kT algorithm with a distance parameter of 0.4. Hence, these jets are called "PUPPIJetAK4", where the effects of pileup are mitigated by means of the PUPPI algorithm [17]. The jet identification criteria used in this analysis are the following:

- jets are required to have $p_T > 30$ GeV and $|\eta| < 2.4$;
- a $\Delta R(jet, lepton) > 0.4$ cut is applied to reject jets overlapping with the candidate leptons;
- at least one of the jets is required to be consistent with originating from b-quarks. For this the default DELPHES b-tagging utility is used.

A further cut is made on missing transverse energy ${E_T}^{miss} > 40$ GeV.

Expected number of observed events in the $e\mu$ channel at a 14 TeV center of mass energy and corresponding to 3000 fb^{-1} of collected data are presented in Table 2. The impacts of major cuts, oppositely charged dilepton requirement (2 leptons), 2 jets isolated from the leptons (2 jets), missing transverse energy requirement (MET), and the b-tag requirement, are presented.

Table 2: Event yields post cuts at 14 TeV and corresponding to 3000 fb^{-1} of data. ϵ_{tot} is the fraction of events remaining after each cut relative to the original sample size, while ϵ_{cut} is the fraction of events remaining after the cut relative to the previous step.

Cut	SUSY	$t\bar{t}$	Single Top	Diboson
2 leptons	3180752	46942286	6291825	875681
$\epsilon_{tot}, \epsilon_{cut}$	14 %, 14 %	14 %, 14 %	2 %, 2 %	9 %, 9 %
2 jets	2230452	34109607	3035953	123486
$\epsilon_{tot}, \epsilon_{cut}$	10 %, 70 %	10 %, 73 %	1 %, 48 %	1 %, 14 %
MET	1867103	27796121	2462018	112145
$\epsilon_{tot}, \epsilon_{cut}$	8 %, 84 %	8 %, 81 %	1 %, 81 %	1 %, 91 %
b-tag	1812201	27133968	2204553	49470
$\epsilon_{tot}, \epsilon_{cut}$	8 %, 97 %	8 %, 98 %	1 %, 90 %	1 %, 44 %

The four-momenta of the top quark and antiquark in each event are estimated using a kinematic reconstruction algorithm [18]. The algorithm considers all possible assignments of reconstructed jets and leptons to the b quarks and leptons from top quark decay, and solves for the unknown neutrino momenta using the following assumptions and constraints: $p_{\mathrm{T}}^{\mathrm{miss}}$ is assumed to originate solely from the two neutrinos; the invariant mass of each reconstructed W boson (m_{W}) is equal to 80.4 GeV [19]; and the invariant mass of each reconstructed top quark is equal to 172.5 GeV.

Effects of detector resolution are accounted for by randomly smearing the measured energies and directions of the reconstructed jets and leptons according to their simulated resolutions. For a given application of the smearing, the solution of the equations for the neutrino momenta yielding the smallest reconstructed $m_{\mathrm{t\bar{t}}}$ is chosen. For each solution, a weight is calculated based on the spectrum of the true invariant mass of the lepton and b jet system from top quark decay at the particle level [20]. The weights are summed over 100 applications of the smearing, and the top quark and antiquark four-momenta are calculated as a weighted average.

Considering only the combinations with more b-tagged jets, the assignment of jets and leptons that yields the maximum sum of weights is chosen. The efficiency of the kinematic reconstruction, defined as the fraction of the selected $\mathrm{t\bar{t}}$ events where a solution is found, is about 96% with a typical disagreement of around 0.2%. Events with no real solution for the neutrino momenta are excluded from further analysis.

5 Measurement of strength of spin correlation

The level of spin correlation in the data is typically quantified by the variable f_{SM}, which refers to the fraction of SM-like spin correlation events as opposed to events with no spin correlation. Therefore f_{SM} represents the strength of the given measure of spin correlation relative to the SM prediction. A linear dependence of f_{SM} on the measured coefficient is defined, where f_{SM} = 1 and f_{SM} = 0 correspond to measurements in agreement with the NLO calculations in the presence and absence of spin correlation, respectively.

A measurement of f_{SM} requires a prediction for the shape of the distribution in the presence and absence of spin correlation. To that end we analyze a 13 TeV $\mathrm{t\bar{t}}$ MC sample generated with top quark spin correlation turned off, applying the same event selection and top reconstruction procedure that we perform on the SM $\mathrm{t\bar{t}}$ sample, described in Section 6.1. We perform a CM energy reweighing on the sample for parity with the 14 TeV $\mathrm{t\bar{t}}$ sample.

Typically, for spin correlation variables in the $\mathrm{t\bar{t}}$ center of mass frame, analytical predictions are used to derive the value of f_{SM}. In this analysis, however, we use the laboratory-frame observables defined above: D, the asymmetry in $\Delta\phi$, $A_{|\Delta\phi|}$, and the asymmetry in $\cos\varphi^{\mathrm{lab}}$, $A^{\mathrm{lab}}_{\cos\varphi}$, and so the MC should suffice as theory predictions. Control plots for these observables and their input variables (in case of D) are provided in Figure 4.

The expression for f_{SM} for a given laboratory-frame variable (say D) is:

$$f_{SM} = \frac{D_{measured} - D_{theory,uncorrelated}}{D_{theory,correlated} - D_{theory,uncorrelated}} \tag{11}$$

In the absence of true data, the expected value for f_{SM} would just be 1. We seek, however, to quantify the uncertainties on the value of f_{SM} that could be extracted from laboratory-frame variables at the HL-LHC.

6 Search for top squark pair production

6.1 Signal and background

Supersymmetry (SUSY) signal samples are generated by employing MADGRAPH5 version 2.2.2. The parton showering and hadronization are carried out with PYTHIA (v8.219) [21]. A DELPHES [22] simulation of the detector is used to model detector response at the HL-LHC.

A scan of 79 different combinations of top squark and neutralino masses is used requiring that $|m_{\tilde{t}_1} - m_{\tilde{\chi}^0_1}| - m_t$ = 0, ±10, ±20 or ±30 GeV with $m_{\tilde{t}_1}$ from 145 to 295 GeV and $m_{\tilde{\chi}^0_1}$ from 0 to 120 GeV in steps of 10 GeV. We refer to this phase space as (low) top quark mass corridor, which is experimentally difficult since the top squark signal has very similar kinematics to the top quark pair production background. In order to extend the phase-space, Monte Carlo (MC) samples with $m_{\tilde{t}_1}$ from 300 to 900 GeV in steps of 50 GeV along the same 7 lines (i.e $|m_{\tilde{t}_1} - m_{\tilde{\chi}^0_1}| - m_t$ = 0, ±10, ±20 or ±30 GeV) in the high top quark mass corridor are also used. The corresponding 14 TeV cross sections, which depend on the top squark mass alone [23], are shown in Figure 3.

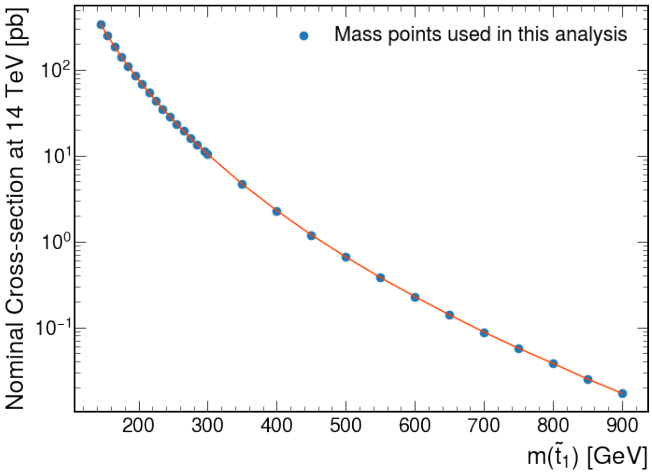

Figure 3: Signal cross sections for top squark pair production with top squark masses between 145 and 900 GeV from [24]. All signal mass points with the same top squark mass have the same cross section. An uncertainty of 14 % is associated on the cross section for each mass point.

The SM background is dominated by $t\bar{t}$ (95%) with a remaining 4.6% single top (tW), 0.3% $t\bar{t}V$, 0.17% VV, and $8 \cdot 10^{-3}$% VVV, where V refers to a vector boson, namely either a Z or a W. All SM processes are simulated using the same tools as the signal samples.

The effects of pileup are estimated by overlaying the hard scatter event with minimum bias events drawn from a $< \mu >$ = 200 Poisson distribution.

6.2 Analysis Strategy

A Deep Neural Network (DNN) is used to separate SM processes from the hypothesized SUSY signal. In this analysis the DNN improves the sensitivity to SUSY signals by about one order of magnitude compared to just using the increase in cross section due to the existence of top squark pair production. In order to avoid training a classifier per mass point, we use a parametric DNN where the top squark and neutralino masses are used as parameters, which allows the NN to learn the correlation between signal and background. For the background samples (dominated by the $t\bar{t}$ process) we assign top squark and neutralino masses with the probability of assignment proportional to the actual probability of the SUSY mass point in the entire sample. We use around 1 million events, with an equal number of signal and background events to avoid any impact of limited MC statistics in the training of the DNN.

The neural network consists of 19 input nodes and a single output node. It includes two hidden layers with a 128 neurons each, with ReLU activations with the exception of the final layer which uses a sigmoid activation [25]. We train with a batch size of 128 for 500 epochs. The loss function of choice is binary cross-entropy, which results in the maximum likelihood estimator in the case of binary classification problems.

For the DNN input nodes we use 19 spin correlation variables. These variables, defined in Section 2, are :

- all 9 elements of the spin correlation matrix C_{ij} defined in the r, k and n basis;
- all 6 spin polarization terms B_i for both the reconstructed top quark and antiquark defined in the r, k and n basis;

- the difference in azimuthal angle ϕ between the two leptons $\Delta\phi_{\ell\ell}$, and their difference in pseudo-rapidity $\Delta\eta_{\ell\ell}$;
- $\cos\varphi$, $\cos\varphi_{\text{lab}}$.

The motivation for using some of these variables can be found in [26]. The highest ranked variables are the angular variables $\Delta\eta_{\ell\ell}$, $\cos\varphi_{\text{lab}}$, and $\Delta\phi_{\ell\ell}$. In principle, adding additional kinematic variables to the DNN will improve the sensitivity further. However, by adding basic kinematic observables such as transverse momenta of leptons and jets, and ${E_T}^{miss}$, we could not improve the sensitivity by more than 5-10% in the corridor investigated. Although top squarks are not expected to alter the polarization of the top quark daughters we add the polarization variables to the DNN since these are mostly uncorrelated with the other spin correlation variables and hence, improve the performance of the DNN. Control plots for the most sensitive DNN inputs are provided in Figure 4, which are the same we employed to extract f_{SM} but in addition also $\Delta\eta_{\ell\ell}$.

The training and test dataset DNN shapes for both the SUSY signal and the SM background are presented in Figure 5 for different mass points. Mass points close to the top mass are harder to discriminate, while those further away are relatively easier. Coupled with the reasonable training curves, we can conclude that no over-training is observed.

7 Systematic Uncertainties

This projection assumes that the CMS experiment will have a similar level of detector and triggering performance during the HL-LHC operation as it provided during the LHC Run 2 period [8–12].

The dominant systematics in this analysis are the theoretical uncertainties due to parton distribution functions (PDF), renormalization and factorization scales, and the uncertainty on the cross-section, primarily in the SUSY signal sample. Some of the systematic uncertainties are applied as simple percentages using the Yellow Report recommendations [1]. These are listed in Table 3.

Table 3: Summary of flat systematic uncertainties.

Systematic Uncertainty	Yellow Report Recommendation
Muon ID	0.5 %
Electron ID	1 %
Luminosity	1 %
b-tagging	1 %
Pile Up	2 %
Theoretical	50 % of current 14 TeV cross-sections

The other shape-based uncertainties are listed in Table 4 and their treatment is discussed in the following sub-sections.

Uncertainties used in the measurement of f_{SM}, the fraction of SM-like spin correlation, are described in Section 7.5.

7.1 PDF Uncertainty

The uncertainty arising from the PDF is assessed by reweighing the samples according to the 100 replicas in the NNPDF3.0 error PDF sets. Variations in α_s are also performed, again using the LHE weights.

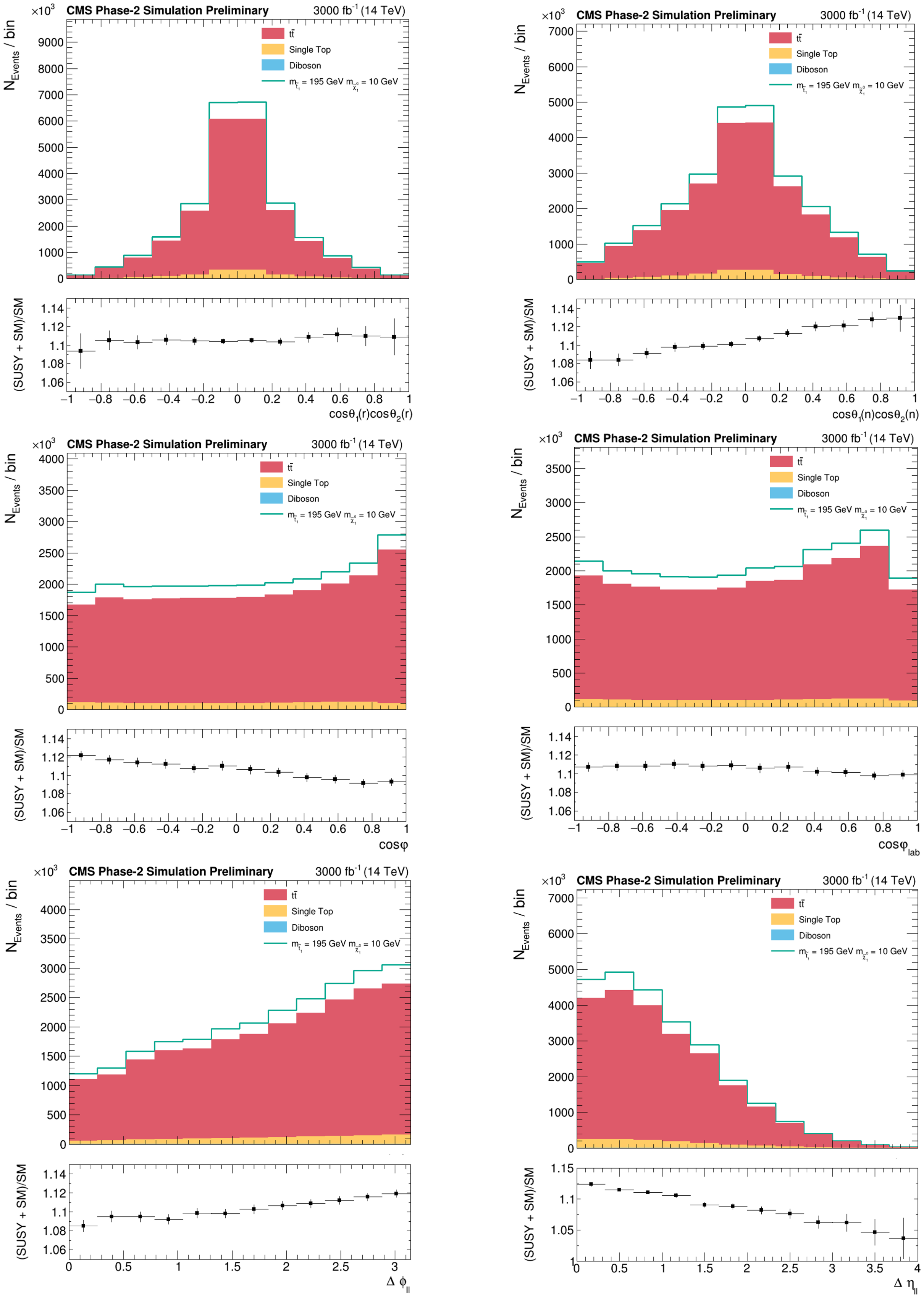

Figure 4: From top to bottom and left to right: diagonal terms of the $t\bar{t}$ spin correlation matrix along the r and n axis; $\cos\varphi$ and $\cos\varphi_{\text{lab}}$; $\Delta\phi$ and $\Delta\eta$ between the leptons. Lower pad shows a ratio of SUSY signal plus SM backgrounds over SM backgrounds, allowing to compare the shape of SUSY prediction versus the SM one.

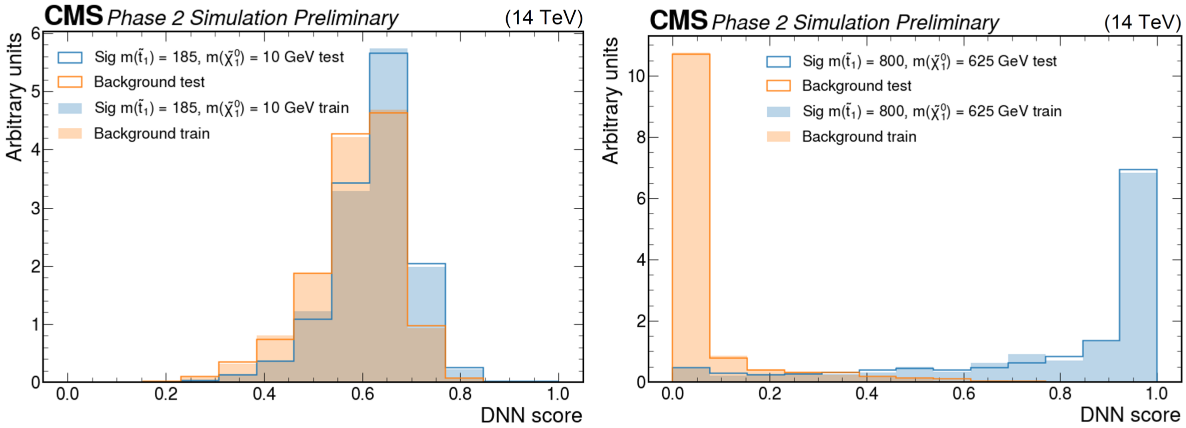

Figure 5: Parametric DNN output for SM background ($t\bar{t}$) and SUSY signal mass points with $m_{\tilde{t}_1}$ = 185 GeV and $m_{\tilde{\chi}_1^0}$ = 10 GeV, and with $m_{\tilde{t}_1}$ = 800 GeV and $m_{\tilde{\chi}_1^0}$ = 625 GeV, respectively.

The Yellow Report guidelines provide a PDF adjustment table [27], which specifies a reduction factor on the basis of the underlying production process (gg, gq or $q\bar{q}$) and M_x (invariant mass of the two partons) in the event. These are looked up from the generator level information and the corresponding correction is applied.

7.2 Top p_T Uncertainty

This uncertainty only applies to the $t\bar{t}$ Monte Carlo. We use the 13 TeV top p_T reweighting function to assess the systematic variation: $e^{p_0 + p_1 \cdot p_T}$, with $p_0 = 0.0615$ and $p_1 = -0.0005$. The geometric average of the top quark and antiquark weights is used as the event weight. Top p_T uncertainty is taken to be 1/3 of what is computed using this Run 2 technique, as suggested in the Yellow Report guidelines.

7.3 JES and JER Uncertainty

For the Jet Energy Scale (JES) uncertainty we use the jet corrections provided in Ref. [28] to correct the jet p_T. These corrections are used to generate 'UP' and 'DOWN' variations. These variations are then used to develop an event weight.

The Jet Energy Resolution (JER) uncertainty is modeled as function of η as suggested in [28]. We see an increase in the cumulative uncertainties at around $|\eta| = 1$, thus we assume a 3% uncertainty until $|\eta| = 1$ and 5% for $|\eta| \geq 1$.

7.4 Scale Uncertainty

Renormalization (μ_R) and factorization (μ_F) scales are varied via the use of LHE weights. A total of 10 variations are constructed by varying μ_F and μ_R between 2 and 0.5 to generate 'UP' and 'DOWN' variations respectively. From the 10 different variations, an envelope for the total scale variation is constructed. The final scale uncertainty quoted is 1/2 of the Run2 estimate.

7.5 Uncertainties for f_{SM} fraction of SM-like spin correlation

To determine the systematic uncertainty on the laboratory-frame variables used in the f_{SM} measurement, we generate UP ($+1\sigma$) and DOWN (-1σ) variations for each systematic described above and then perform a weighted average across all bins to find the mean uncertainty due to that systematic. This procedure is repeated for all systematics, for both correlated and uncorrelated samples.

Table 4: Summary of shape-based systematic uncertainties.

Systematic Uncertainty	Yellow Report Recommendation
PDF	M_x based look-up table
top p_T	33% of Run2
Jet Energy Scale	from shape (using [1])
Jet Energy Resolution	from shape (using [1])
Renormalization and Factorization Scale	50 % of Run2

Theory uncertainties are obtained from [4] and are reduced by 50% as per Yellow Report recommendations.
Systematic uncertainties are treated as uncorrelated and added in quadrature to obtain the final numbers for all of the above mentioned laboratory-frame variables. Finally, the uncertainties are propagated through the expression for f_{SM}.

8 Results

8.1 Expected results for spin correlation measurement

Figure 6 shows the projection of a measurement of the strength of the SM spin correlation in 14 TeV proton-proton collisions using different variables. We compare the projected results to existing values of the same variables extracted at 13 TeV by CMS [29] and ATLAS [30].

Unprecedented precision in measuring spin correlation variables is expected, with D the most accurate variable with a 3% total uncertainty.

A deviation of $|\Delta\phi|$ of 2.2 standard deviation was seen in the ATLAS Run 2 measurement [30], while this excess was not seen in CMS [29]. With this projection we will fully solve this puzzle because our expected accuracy is much smaller than the existing level of deviation from the SM. Thus, we will either confirm the deviation and make a discovery of beyond the SM physics contributions, or reject it.

8.2 Expected results for search for top squark pair production

Figure 7 presents the output of the trained DNN on the test data set for two different top squark mass points: 225 and 550 GeV. For each top squark mass point, a binned likelihood fit is performed with 10000 pseudo experiments in order to determine the 5σ discovery potential in the top squark-neutralino mass plane. In the absence of a discovery we derive the median ($\pm 2\sigma$) upper expected limit. Corresponding to each top squark mass point there is a neutralino mass such that $\Delta M(\tilde{t}_1, \tilde{\chi}_1^0) = 175$ GeV.

In the absence of a non-SM signal this analysis projects to exclude the top squark and neutralino mass corridor up to masses of 600 GeV, which is similar to existing expected exclusion limits in Run 2 data[31]. These expected limits are derived by a DNN method relying on kinematic and event-based input variables. However, the use of spin correlation variables and the unprecedented data statistics of the HL-LHC phase allow to target the top squark and neutralino mass corridor below 300 GeV with greater sensitivity. At a top squark mass of 195 GeV (275 GeV) and $\Delta M(\tilde{t}_1, \tilde{\chi}_1^0) = 175$ GeV, for example, the existing expected upper limit on the cross section is 42 pb (8pb) [31], while in our analysis we achieve 0.96 pb (0.90 pb). Therefore, existing upper limits on the top squark pair production cross section at low top squark masses (< 300 GeV)

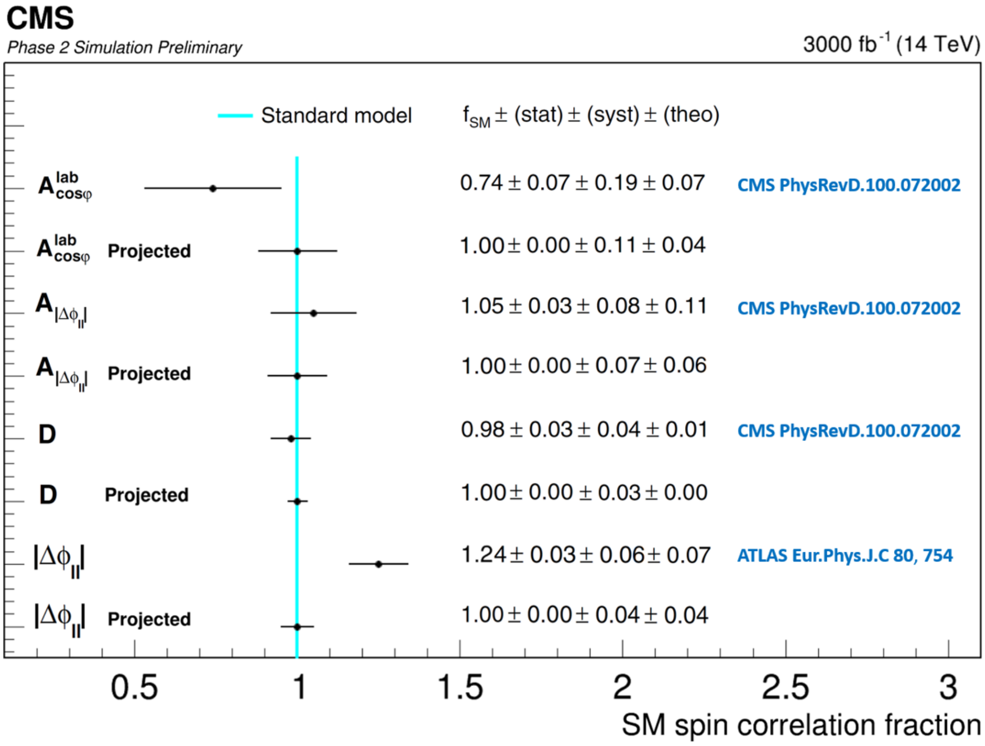

Figure 6: Extracted values of f_{SM} from laboratory-frame spin correlation variables by CMS [29] and ATLAS [30] at 13 TeV and projected values at 14 TeV. The measured and projected values with their statistical, systematic, and theoretical uncertainties are given on the right. Statistical uncertainties of the data on the projected values are smaller than 0.004 and hence, denoted with 0.00. As per Yellow Report recommendations theory uncertainties are reduced by 50% for projected values.

will be improved by about one order of magnitude.

An expected discovery sensitivity is calculated using the asymptotic formulae [32] of the CLs criterion [33]. Signals are expteced to be discovered when the mean expected observation for a signal model lies above the 99.9999713 percentile (5σ single sided equivalent) for the standard-model-only distribution. Conversely, expected upper limits at the 95% confidence level (CL) are determined when the standard-model-only value of the signal strength parameter is below the 5^{th} percentile of pseudo-experiments from the signal.

The region of discovery potential in the top squark and neutralino mass plane is shown in Figure 8. In the absence of a signal we will be able to exclude the top squark phase space in that region.

Figure 9 shows the expected limits on the SUSY cross-section in the 2D top squark mass and neutralino mass plane.

Figure 10 shows expected limits on the SUSY cross-sections for different top squark masses, as explained in Section 4, and a neutralino mass point such that $\Delta M(\tilde{t}_1, \tilde{\chi}_1^0) = 175$ GeV. The dashed red line is the predicted NLO + NLL SUSY cross-section. In deriving these limits, a 100% branching ratio of top squark to top quark is assumed. Uncertainties arising from limited statistics in the MC samples are not considered in deriving these limits. Expected limits on the SUSY cross-sections for different top squark masses and a neutralino mass point such that $\Delta M(\tilde{t}_1, \tilde{\chi}_1^0) = 145, 155, 165, 185, 195,$ and 205 GeV, are presented in the Appendix.

We see that the nominal final dataset of 3 ab^{-1} of 14 TeV proton-proton collisions will be able to discover a non-SM signal in the relevant phase space. In the absence of a non-SM signal this analysis can exclude the top squark and neutralino mass corridor up to masses of 600 GeV. Compared to a existing Run 2 analysis [31] we will push down the existing limits for the top squark and neutralino mass corridor with masses less than 300 GeV by one order of magnitude. With the full 3000 fb^{-1} dataset and the proposed reduction in uncertainties, the CMS experiment could achieve 5σ discovery sensitivity for top squark masses up to 400 GeV in the presence of a SUSY signal. In the absence of a signal, top squarks with masses up to 600 GeV could be excluded at 2σ confidence.

Figure 11 shows the ratio of exclusion limits of the combined search for top squarks from Ref. [31] to the ones derived in the context of this search for the low top squark-neutralino mass plane. It clearly shows the significant improvement between 2-50 in sensitivity and exclusion limits of the high-lumi data set to hypothetical top quark partner particles. This performance allows discovery (or exclusion) even in much less favorable top squark decays or in the case of branching fractions for top squark to top quark decays being $\ll 1$.

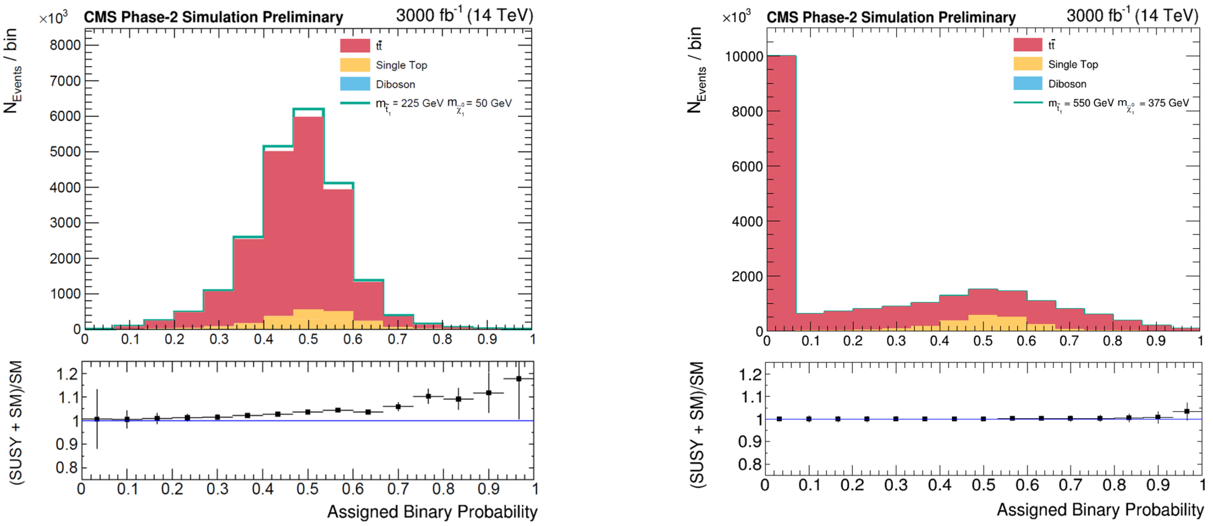

Figure 7: DNN output on the test datasets for two different top squark masses : 225 and 550 GeV.

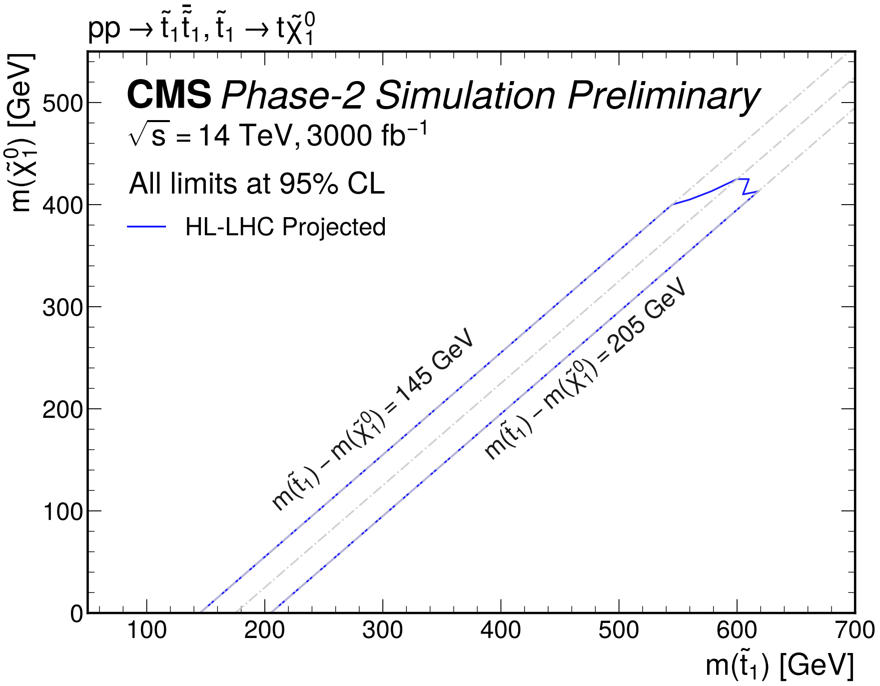

Figure 8: Projected region of discovery potential in the top squark and neutralino mass plane. The center line corresponds to $\Delta M(\tilde{t}_1, \tilde{\chi}_1^0) = 175$ GeV.

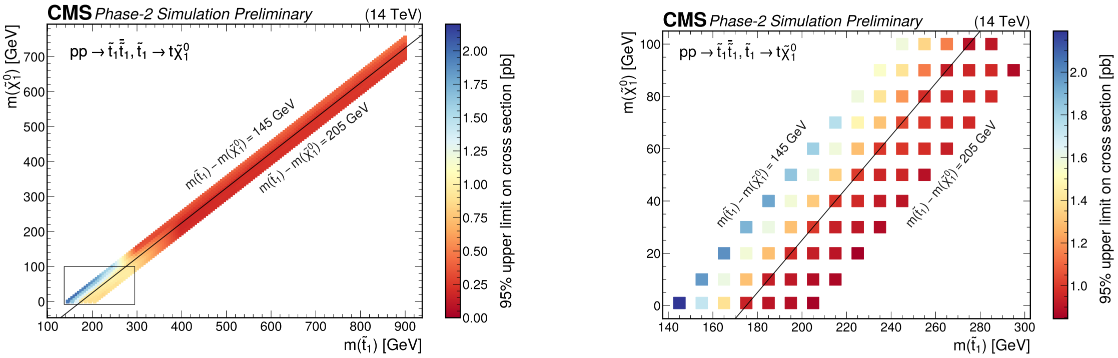

Figure 9: Expected 95 % CL upper limits on the SUSY cross section (in pb) as a function of the top squark and neutralino masses in the top quark corridor region (left). We highlight the limits (right) in the already excluded region in the low top squark-neutralino mass plane. In both plots we add a center line to guide the eye, which corresponds to $\Delta M(\tilde{t}_1, \tilde{\chi}^0_1) = 175$ GeV.

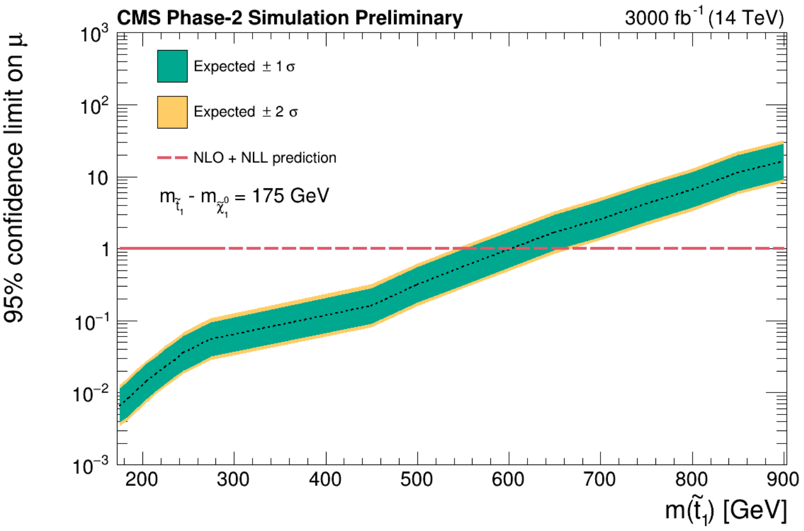

Figure 10: Expected limits on signal strength calculated using asymptotic formulae. Corresponding to each top squark mass point there is a neutralino mass such that $\Delta M(\tilde{t}_1, \tilde{\chi}^0_1) = 175$ GeV. The green and yellow bands represent the regions containing 68% and 95%, respectively, of the expected limits. The red dashed line indicates the approximate NLO+NLL prediction.

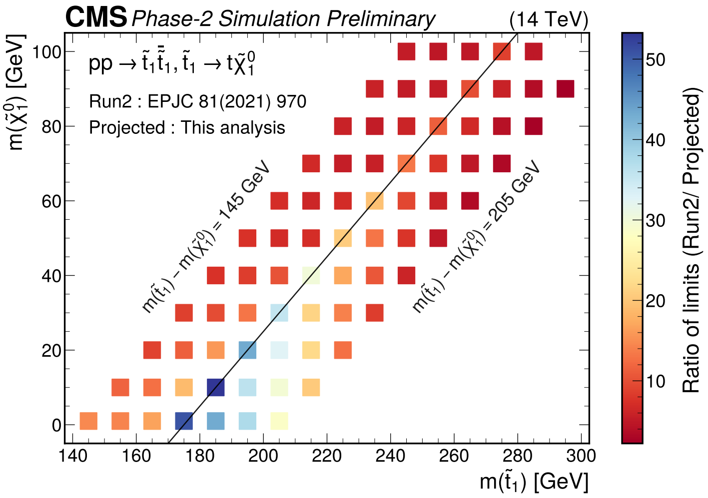

Figure 11: Ratio of expected 95% CL upper limits of the combined search for top squarks from Ref. [31] to the ones derived in the context of this search for the low top squark-neutralino mass plane. The center line corresponds to $\Delta M(\tilde{t}_1, \tilde{\chi}_1^0) = 175$ GeV.

9 Conclusions

In this analysis we present a first study of the performance of the expected precision of a measurement of the strength of expected $t\bar{t}$ spin correlation in 14 TeV proton-proton collisions. Unprecedented precision in measuring spin correlation variables is expected, with D the most accurate variable with a 3% total uncertainty.

We also presented a Deep Neural Network (DNN) based approach to searches for new physics in the low and high top quark mass corridor using top quark spin correlation. Using this method alone and extending the corridor up to masses in the 1 TeV range, we can significantly increase the ultimate reach of the LHC to discover top squarks in the degenerate mass corridor in the top squark-neutralino plane, or in the absence of a discovery exclude top squarks up to 600 GeV. In particular, in the top squark and neutralino mass corridor existing top squark pair production cross section limits can be improved by about one order of magnitude for top squark masses less than 300 GeV. Naturalness arguments still hint at the low top squark mass phase space region as a less fine-tuned implementation of SUSY, which so far might have escaped discovery given the abundance of top quarks in the same phase space folded with less favorable SUSY scenarios.

In principle, adding more kinematic variables to the DNN will improve the sensitivity further by an additional 5-10%. However, the purpose of this analysis is to show that $\mathrm{t\bar{t}}$ spin correlation variables will be an important asset for any type of searches for new physics involving top quark pairs. This is especially true for corners of the phase space that are difficult to access by classical searches using only kinematic variables in the low top quark mass corridor. This phase space represents less fine-tuned implementations of beyond the SM SUSY models.

Given the model independent nature of this channel, other new physics signatures may be probed by this approach and make ample use of the ultimate 3 ab^{-1} dataset.

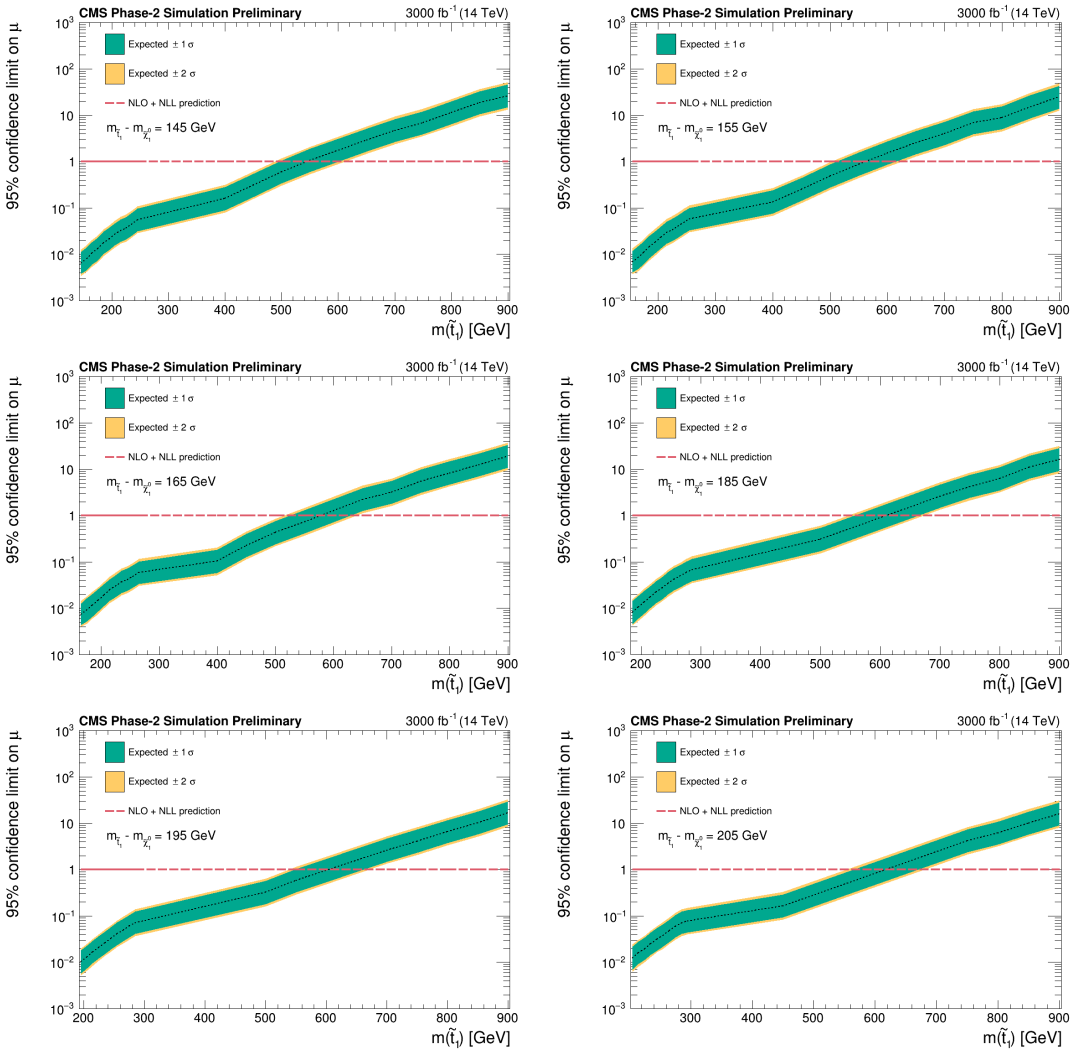

Figure 12: Expected limits on signal strength calculated using asymptotic formulae. Corresponding to each top squark mass point there is a neutralino mass such that $\Delta M(\tilde{t}_1, \tilde{\chi}_1^0) = 145$ GeV (top left), $\Delta M(\tilde{t}_1, \tilde{\chi}_1^0) = 155$ GeV (top right), $\Delta M(\tilde{t}_1, \tilde{\chi}_1^0) = 165$ GeV (middle left), $\Delta M(\tilde{t}_1, \tilde{\chi}_1^0) = 185$ GeV (middle right), $\Delta M(\tilde{t}_1, \tilde{\chi}_1^0) = 195$ GeV (bottom left), $\Delta M(\tilde{t}_1, \tilde{\chi}_1^0) = 205$ GeV (bottom right). The green and yellow bands represent the regions containing 68% and 95%, respectively, of the expected limits. The red dashed line indicates the approximate NLO+NLL prediction.

10 Appendix

The plots in Figure 12 show expected limits on the SUSY cross-sections for different top squark masses, as explained in Section 4, and a neutralino mass point such that $\Delta M(\tilde{t}_1, \tilde{\chi}_1^0) = 145, 155,$ $165, 185, 195,$ and 205 GeV, respectively.

References

[1] CMS Phase II Upgrade Performance Studies Group Collaboration, "TWiki: Recommendations for Systematic Uncertainties HL-LHC (3 fb-1)", CMS twiki pages v1, 2021.

[2] M. Baumgart and B. Tweedie, "A new twist on top quark spin correlations", *bib:1212.4888* (2013), no. 3, `doi:10.1007/JHEP03(2013)117`, `arXiv:1212.4888`.

[3] C. Degrande et al., "Non-resonant new physics in top pair production at hadron colliders", *JHEP* **03** (2011) 125, `doi:10.1007/JHEP03(2011)125`, `arXiv:1010.6304`.

[4] W. Bernreuther, D. Heisler, and Z.-G. Si, "A set of top quark spin correlation and polarization observables for the LHC: Standard model predictions and new physics contributions", *JHEP* **12** (2015) 026, `doi:10.1007/JHEP12(2015)026`, `arXiv:1508.05271`.

[5] G. Mahlon and S. J. Parke, "Spin correlation effects in top quark pair production at the LHC", *Phys. Rev. D* **81** (2010) 074024, `doi:10.1103/PhysRevD.81.074024`, `arXiv:1001.3422`.

[6] A. Brandenburg, Z.-G. Si, and P. Uwer, "QCD-corrected spin analysing power of jets in decays of polarized top quarks", *Phys. Lett. B* **539** (2002) 235, `doi:10.1016/S0370-2693(02)02098-1`, `arXiv:hep-ph/0205023`.

[7] CMS Collaboration, "The CMS Experiment at the CERN LHC", *JINST* **3** (2008) S08004, `doi:10.1088/1748-0221/3/08/S08004`.

[8] CMS Collaboration, "Technical Proposal for the Phase-II Upgrade of the CMS Detector", CMS Technical Proposal CERN-LHCC-2015-010. LHCC-P-008. CMS-TDR-15-02, 2015.

[9] CMS Collaboration, "The Phase-2 Upgrade of the CMS Tracker", CMS Technical Design Report CERN-LHCC-2017-009. CMS-TDR-014, 2017.

[10] CMS Collaboration, "The Phase-2 Upgrade of the CMS Barrel Calorimeters Technical Design Report", CMS Technical Design Report CERN-LHCC-2017-011. CMS-TDR-015, 2017.

[11] CMS Collaboration, "The Phase-2 Upgrade of the CMS Endcap Calorimeter", CMS Technical Design Report CERN-LHCC-2017-023. CMS-TDR-019, 2017.

[12] CMS Collaboration, "The Phase-2 Upgrade of the CMS Muon Detectors", CMS Technical Design Report CERN-LHCC-2017-012. CMS-TDR-016, 2017.

[13] C. CMS, "A MIP Timing Detector for the CMS Phase-2 Upgrade", technical report, CERN, Geneva, Mar, 2019.

[14] CMS Collaboration, "The Phase-2 Upgrade of the CMS Level-1 Trigger", technical report, CERN, Geneva, Apr, 2020. Final version.

[15] C. Collaboration, "The Phase-2 Upgrade of the CMS Data Acquisition and High Level Trigger", technical report, CERN, Geneva, Mar, 2021. This is a temporary submission, just to get the LHCC reference number, to be used in this and other CMS documents.

[16] CMS Collaboration, "Expected performance of the physics objects with the upgraded CMS detector at the HL-LHC", Technical Report CMS-NOTE-2018-006. CERN-CMS-NOTE-2018-006, 2018.

[17] CMS Collaboration, "Pileup mitigation at CMS in 13 TeV data", *JINST* **15** (2020), no. 09, P09018, `doi:10.1088/1748-0221/15/09/P09018`, `arXiv:2003.00503`.

[18] B. A. Betchart, R. Demina, and A. Harel, "Analytic solutions for neutrino momenta in decay of top quarks", *Nuclear Instruments and Methods in Physics Research Section A: Accelerators, Spectrometers, Detectors and Associated Equipment* **736** (Feb, 2014) 169178, `doi:10.1016/j.nima.2013.10.039`.

[19] Particle Data Group, "Review of particle physics", *Phys. Rev. D* **98** (2018) 030001, `doi:10.1103/PhysRevD.98.030001`.

[20] CMS Collaboration, "Measurements of $\mathrm{t\bar{t}}$ differential cross sections in proton-proton collisions at $\sqrt{s} = 13$ TeV using events containing two leptons", *JHEP* **02** (2019) 149, `doi:10.1007/JHEP02(2019)149`, `arXiv:1811.06625`.

[21] T. Sjöstrand et al., "An introduction to PYTHIA 8.2", *Comput. Phys. Commun.* **191** (2015) 159, `doi:10.1016/j.cpc.2015.01.024`, `arXiv:1410.3012`.

[22] DELPHES 3 Collaboration, "DELPHES 3, A modular framework for fast simulation of a generic collider experiment", *JHEP* **02** (2014) 057, `doi:10.1007/JHEP02(2014)057`, `arXiv:1307.6346`.

[23] LHC SUSY Cross Section Working Group Collaboration, "TWiki: stop/sbottom cross section with squarks and gluinos decoupled", CMS twiki pages v1, 2021.

[24] CMS Phase II Upgrade Performance Studies Group Collaboration, "TWiki: SUSY Cross Sections at 14 TeV for stop/sbottom", CMS twiki pages v1, 2021.

[25] F. Chollet et al., "Keras", technical report, 2015.

[26] Z. Han, A. Katz, D. Krohn, and M. Reece, "(light) stop signs", *Journal of High Energy Physics* **2012** (Aug, 2012) `doi:10.1007/jhep08(2012)083`.

[27] CMS Phase II Upgrade Performance Studies Group Collaboration, "TWiki: PDFs HL-LHC Summary Table", CMS twiki pages v1, 2021.

[28] Yellow Report Systematics. `https://twiki.cern.ch/twiki/bin/viewauth/CMS/Internal/TdrProcessing`.

[29] CMS Collaboration, "Measurement of the top quark polarization and $\mathrm{t\bar{t}}$ spin correlations using dilepton final states in proton-proton collisions at $\sqrt{s} = 13$ TeV", *Phys. Rev. D* **100** (2019), no. 7, 072002, `doi:10.1103/PhysRevD.100.072002`, `arXiv:1907.03729`.

[30] ATLAS Collaboration, "Measurements of top-quark pair spin correlations in the $e\mu$ channel at $\sqrt{s} = 13$ TeV using pp collisions in the ATLAS detector", *Eur. Phys. J. C* **80** (2020), no. 8, 754, `doi:10.1140/epjc/s10052-020-8181-6`, `arXiv:1903.07570`.

[31] CMS Collaboration, "Combined searches for the production of supersymmetric top quark partners in proton–proton collisions at $\sqrt{s} = 13$ TeV", *Eur. Phys. J. C* **81** (2021), no. 11, 970, `doi:10.1140/epjc/s10052-021-09721-5`, `arXiv:2107.10892`.

[32] G. Cowan, K. Cranmer, E. Gross, and O. Vitells, "Asymptotic formulae for likelihood-based tests of new physics", *Eur. Phys. J. C* **71** (2011) 1554, `doi:10.1140/epjc/s10052-011-1554-0`, `arXiv:1007.1727`. [Erratum: `doi:10.1140/epjc/s10052-013-2501-z`].

[33] A. L. Read, "Presentation of search results: the CL_s technique", *J. Phys. G* **28** (2002) 2693, `doi:10.1088/0954-3899/28/10/313`.